

Potassium Metal Batteries

Unraveling Electrode Surface Chemistry in Determining Interphase Stability and Deposition Homogeneity for Anode-Free Potassium Metal Batteries

Zhenlu Yu, Qun Liu, Danni Wang, Jie Shi, Dengyun Zhai, and Biao Zhang*

Abstract: Potassium metal batteries with an anode-less/-free configuration could realize competitive energy density, which requires exceptional potassium plating/stripping reversibility via guiding smooth potassium growth and building mechanically stable solid electrolyte interphase (SEI). Electrolyte engineering has been the most widely adopted strategy, but there is less understanding of the electrode effect. We demonstrate that the extent of electrolyte decomposition could also be regulated through electrode surface modification. Elevating the work function of an Al current collector by coating a thin layer of Ni-decorated carbon nanofiber could greatly suppress the copious solvent reduction, leading to the formation of inorganic-rich SEIs. Such SEIs possess a large elastic deformation energy to accommodate the volume change and a high ionic conductivity to boost the reaction kinetics. Moreover, the potassiophilic nickel species offer abundant active sites to induce homogeneous potassium deposition. Benefiting from the synergy of stable interphases and promoted nucleation, the modified Al enables a 4.4 V anode-free cell in a normal-concentration electrolyte without anode precycling.

Introduction


Benefiting from the large abundance (~ 2.1 wt.% of earth's crust), high theoretical capacity (687 mA h g^{-1}), low redox potential (-2.93 V vs SHE), and anode compatibility with Al current collector, potassium metal batteries (PMBs) are considered compelling supplements to lithium-based batteries in large-scale energy storage.^[1] Nonetheless, the poor cyclic stability and the inferior reversibility hinder the practical application of PMBs, mostly attributed to unstable SEI^[2] and uncontrollable potassium dendrite growth.^[3] The SEI serves as the ionic conductive but electronic isolating medium between the anode and electrolyte, inhibiting excessive electrolyte decomposition and protecting electrode integrity. A variety of modifications have been put forward to strengthen the stability of SEIs via modulating their composition, including electrolyte design^[4,5] and employment of artificial protecting coatings.^[6,7] Previous research concludes that a high content of inorganic species in a continuous and thin SEI layer is preferable for K metal stability, which is normally achieved through regulating the electrolyte solvation structure.^[8] Such a positive effect of electrolyte regulation is confirmed in graphite-based potassium ion batteries as well.^[9,10] However, little attention is paid to the origin of SEI generation from the aspect of electron convey from the anode (or current collector in anode-free cells) toward electrolytes.


The electrolyte remains thermodynamically stable within its electrochemical window and will undergo reduction or oxidization to form a passivating interphase beyond this potential range.^[11] Upon the K plating period, the electric potential of the anode will decrease, accompanied by an increase in the Fermi level (E_f) of the anode.^[12–14] Once the E_f of the anode surpasses the energy level associated with the reduction potential of the electrolyte (E_r), electrons will flow from E_f to E_r due to the positive energy gap, resulting in the decomposition of anions and solvents. Reducing the E_f of the anode is expected to narrow such a gap, thereby suppressing the severe electrolyte decomposition. In an anode-free cell, the current collector serves as the anode at the beginning of discharge, thus playing a critical role in SEI formation. This is well illustrated in previous works where the current collector with a lower Fermi level effectively inhibits copious electrolyte reduction and promotes the generation of inorganic SEI.^[15–18]

Apart from the nanostructure of SEI, the K metal deposition morphology could also affect its stability. The dendrite arising from the heterogeneous K growth may break the

[*] Z. Yu, Q. Liu, D. Wang, J. Shi, B. Zhang
 Department of Applied Physics and Research Institute for Advanced Manufacturing, The Hong Kong Polytechnic University, Kowloon, Hong Kong 999077, China
 E-mail: biao.ap.zhang@polyu.edu.hk

D. Zhai
 Shenzhen Geim Graphene Center, Institute of Materials Research, Tsinghua Shenzhen International Graduate School, Tsinghua University, Shenzhen 518055, China

 Additional supporting information can be found online in the Supporting Information section

 © 2025 The Author(s). Angewandte Chemie International Edition published by Wiley-VCH GmbH. This is an open access article under the terms of the [Creative Commons Attribution-NonCommercial-NoDerivs](https://creativecommons.org/licenses/by-nc-nd/4.0/) License, which permits use and distribution in any medium, provided the original work is properly cited, the use is non-commercial and no modifications or adaptations are made.

SEI, leading to the reformation in the subsequent cycles that consume the active K ions and electrolytes. Therefore, guiding smooth K metal growth through increasing the nucleation sites and manipulating the ionic flux on the anode surface is equally important. Incorporating potassiophilic species in the current collector,^[19] introducing inert coating layers on the K metal surface,^[20] building three-dimensional skeletons,^[21,22] and designing the cycling protocol in the first several cycles^[23] are proven as effective strategies to control nucleation behaviors. In particular, tuning the surface functionality of the current collector by carbonaceous materials to decrease the nucleation barrier and prevent dendrite growth is of great interest as it aligns with mass production.^[24,25] Compared to building 3D carbon-based skeletons with larger surface areas,^[21,22] such a thin layer coating of carbonaceous materials on the current collector reduces the risk of side reactions, thereby enhancing the Coulombic efficiency (CE).^[16] Nevertheless, the performance is still unsatisfactory and normally requires the utilization of high-concentration electrolytes.

Considering the above two main factors in stabilizing the SEIs, we design a decorated Al current collector by directly spraying nickel-embedded carbon nanofibers (CNFNi@Al). The CNFNi@Al with a lower Fermi level than bare Al induces a thin inorganic-rich SEI structure with high elasticity. The higher K ion reduction potential, confirmed in a three-electrode cell with two separated K metals as the counter and reference electrode to avoid interference from the counter electrode (Figure 1a), prevents the copious electrolyte decomposition. Additionally, potassiophilic nickel species promote the smooth lateral plating behavior of K metal to suppress dendrite formation. Stemming from the regulated stable SEI with facilitated planar K growth, the CNFNi endows the asymmetric cell with an average CE (ACE) of 99.2% and a duration of over 1500 h in a 1 M electrolyte. Even under a harsh anode-free condition with the high-voltage cathode Mn-based Prussian blue analog (MnHCF), it guarantees the operation of 50 cycles with a specific energy density of 381 Wh kg⁻¹ (based on the MnHCF and CNFNi mass) without anode precycling.

Results and Discussion

Surface Functionality of CNFNi@Al

The synthesis procedure of CNFNi@Al current collector involves electrospinning of CNF, the chemical growth of nickel species on CNF to produce CNFNi, and uniformly spray painting the Al foil with CNFNi dispersion (Figure 1b). Energy-dispersive X-ray spectroscopy (Figure S1) indicates the distribution of Ni elements on CNF after the chemical reduction process. The nickel species of Ni₃N, NiO, and metallic Ni particles with sizes of around 20 nm are generated on CNF with a diameter of around 200 nm, as shown in transmission electron microscopy (TEM) images (Figure 1c and Figure S2). These can be confirmed by the selected area electron diffraction (SAED) pattern (Figure 1d). Multiple pairs of diffraction spots emerge on the pattern of CNFNi samples that can be indexed as the Ni, NiO, Ni₃N, and Ni₃C species.

The NiO is formed from the oxidation of Ni particles, and Ni₃N stems from the reaction between the NiCl₂ solution and N₂H₄ reductant during the chemical reduction procedure. They are expected to exhibit a high affinity to K according to previous reports.^[26,27] A few Ni₃C species should be derived from the interaction between Ni²⁺ and carbon atoms on the CNF matrix. It is found that with the introduction of Ni species, the ratio of D band to G band intensity (I_D/I_G) decreased from 1.03 to 0.98 from Raman patterns (Figure S3a). This originates from the catalysis effect of Ni species to increase the crystallinity of CNF.^[28] The presence of Ni-N, Ni-O, Ni-C, and Ni⁰ peaks in the X-ray photoelectron spectroscopy (XPS) pattern supports the above results as well (Figure S3b,c). Based on the thermogravimetric analysis results (Figure S3d), the amount of overall Ni species in CNFNi is estimated to be 34 wt.%. Most of them are presented in terms of metallic Ni, as indicated by the X-ray diffraction (XRD) results (Figure S4). Compared to Al, Cu, and Fe, the lowest potassium nucleation overpotential on the Ni metal substrate has been observed. The Ni current collector also induces the K plating along with {110} direction (Figure S5). The K {110} plane possesses the lowest surface energy in the body-centered cubic K and the lowest barrier for K atom migration.^[29] Therefore, the presence of these nickel species would decrease the nucleation barrier when CNFNi@Al servers as the current collector.

XPS was carried out to verify the bonding information of CNFNi@Al. The Al-C bonding (Figure S6) implies the presence of coupling between CNFNi and the Al current collector. Contact angle measurements were then employed between bare or spray-coated Al foils and the 1 M bis(fluorosulfonyl)imide potassium/ethylene glycol diethyl ether (1 M KFSI/DEE) electrolyte (Figure 1e), which is selected for its superior stability toward the K anode according to our previous work.^[30] CNFNi@Al exhibits better wettability with a lower contact angle of 10.9°, which guarantees the electrolyte contact and promotes uniform SEI generation.^[31] Additionally, the dropping angle of molten K on CNFNi@Al is 35.2° (Figure S7), much smaller than that of Al (90.1°), indicating the improved K affinity.

The work function (Φ) values of different current collectors were determined by ultraviolet photoelectron spectroscopy (UPS) (Figure 1f and Figure S8). Compared to bare Al foil, the bare CNF-coated Al foil (denoted as CNF@Al) and CNFNi@Al possess high work function values of 3.97 and 4.2 eV, respectively, which corresponds to a low E_f for CNF@Al and CNFNi@Al ($\Phi = E_{\text{vac}} - E_f$, $E_{\text{vac}} = 0$ eV).^[32] It can be ascribed to the higher electronegativity of Ni and CNF than Al,^[33,34] causing a lower electron density for modified Al. Upon discharging of the asymmetric cells coupled with K as the counter electrode, the Fermi level of current collectors undergoes an ascending trend (Figure 1g) as a result of electron rearrangement on the current collector.^[35] The E_f positions of CNF@Al and CNFNi@Al are constantly lower than that of Al regardless of the discharging depth. A narrowed energy gap between E_f and E_r is favorable for restricting the excessive consumption of electrolytes and regulating SEI ingredients. It can be explained by the tunneling theory in quantum mechanics.^[32,36] The tunneling

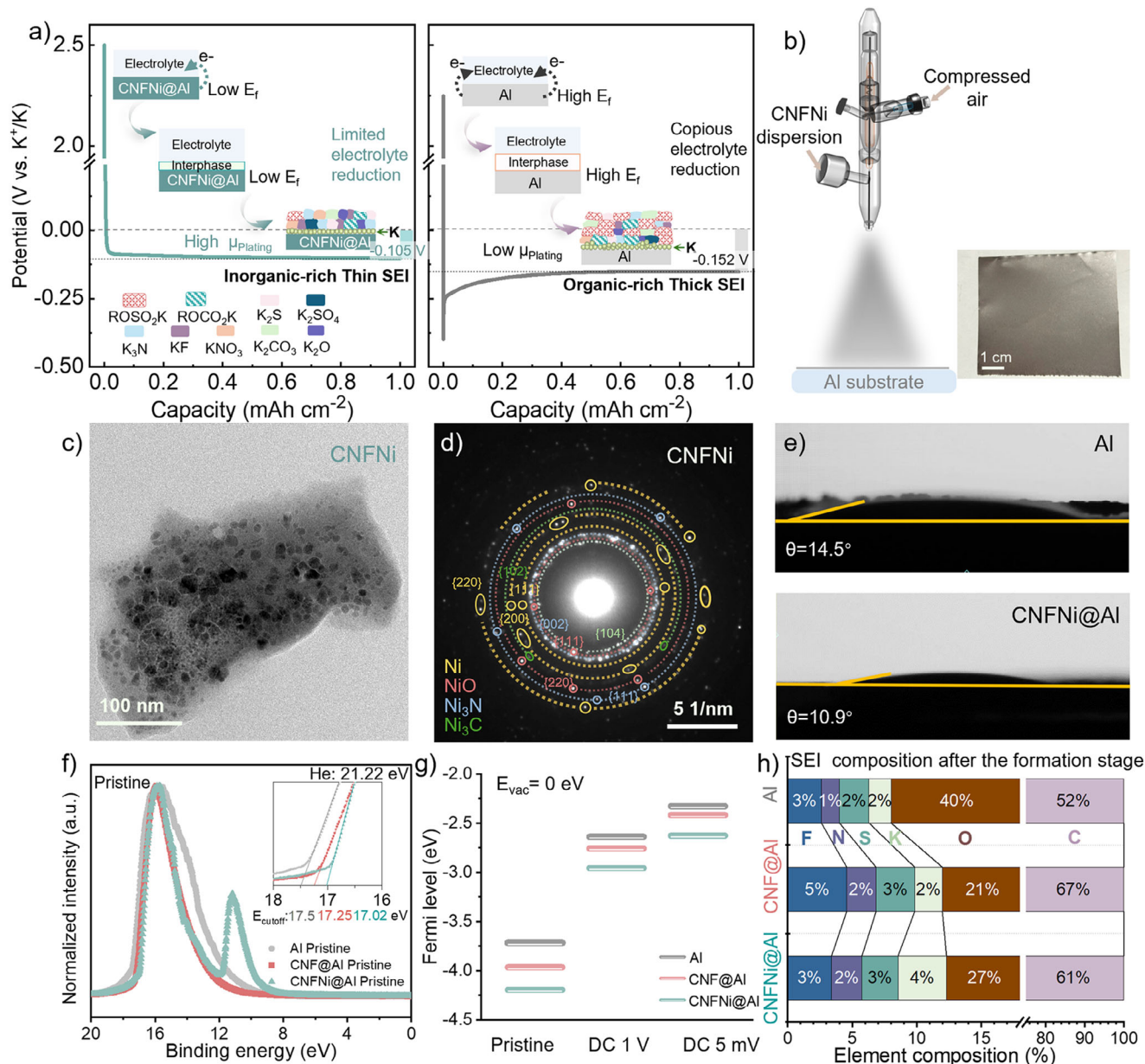


Figure 1. Surface functionality of current collectors. a) Scheme of SEI formation on different current collectors upon 1st K plating in a three-electrode system without formation period. E_f : Fermi level. b) Illustration of spray painting for CNFNI@Al with the photograph. c) Morphology and d) SAED patterns of CNFNI. e) Wetting angles of the 1 M KFSI/DEE electrolyte on Al and CNFNI@Al. f) UPS curves to determine the work functions. g) Calculated Fermi-level positions based on work function. h) Element composition of SEIs generated after three formation cycles.

probability (T) is proportional to $e^{-t\sqrt{\Delta E_t}}$, where ΔE_t indicates the energy difference between the minimum conduction band of SEI and the E_f , and t is the thickness of SEI. With large T , the electron tunneling from SEI to electrolyte will cause continuous loss of electrolytes. Known that a decreased E_f will lead to an increased ΔE_t , the lower E_f for CNFNI@Al would exhibit lower T . It would achieve the electric insulation with a smaller thickness t of SEI.

To verify this assumption, we probe compositions of SEI generated on different current collectors after three formation cycles between 5 mV–1 V under the current density of 0.05 mA cm^{-2} . The overall percentages of elements are

first compared (Figure 1h). Generally, F, N, S, and K elements stem from the reduction products of $[K^+FSI^-]$ and the C element comes from the solvent reduction. Both anions and solvents reduction can generate O-containing products but solvents are the main contributors.^[37] Considering the possible interference of carbon from CNFs on modified Al and the N signal from Ni_3N in CNFNI, we mainly compare the amount of F, S, and K elements. They account for a higher relative content for CNF@Al and CNFNI@Al samples compared to bare Al, suggesting more anion reduction on the modified Al with a lower Fermi level, and implicating the role of CNF in modulating the SEI formation. The sharp decrease

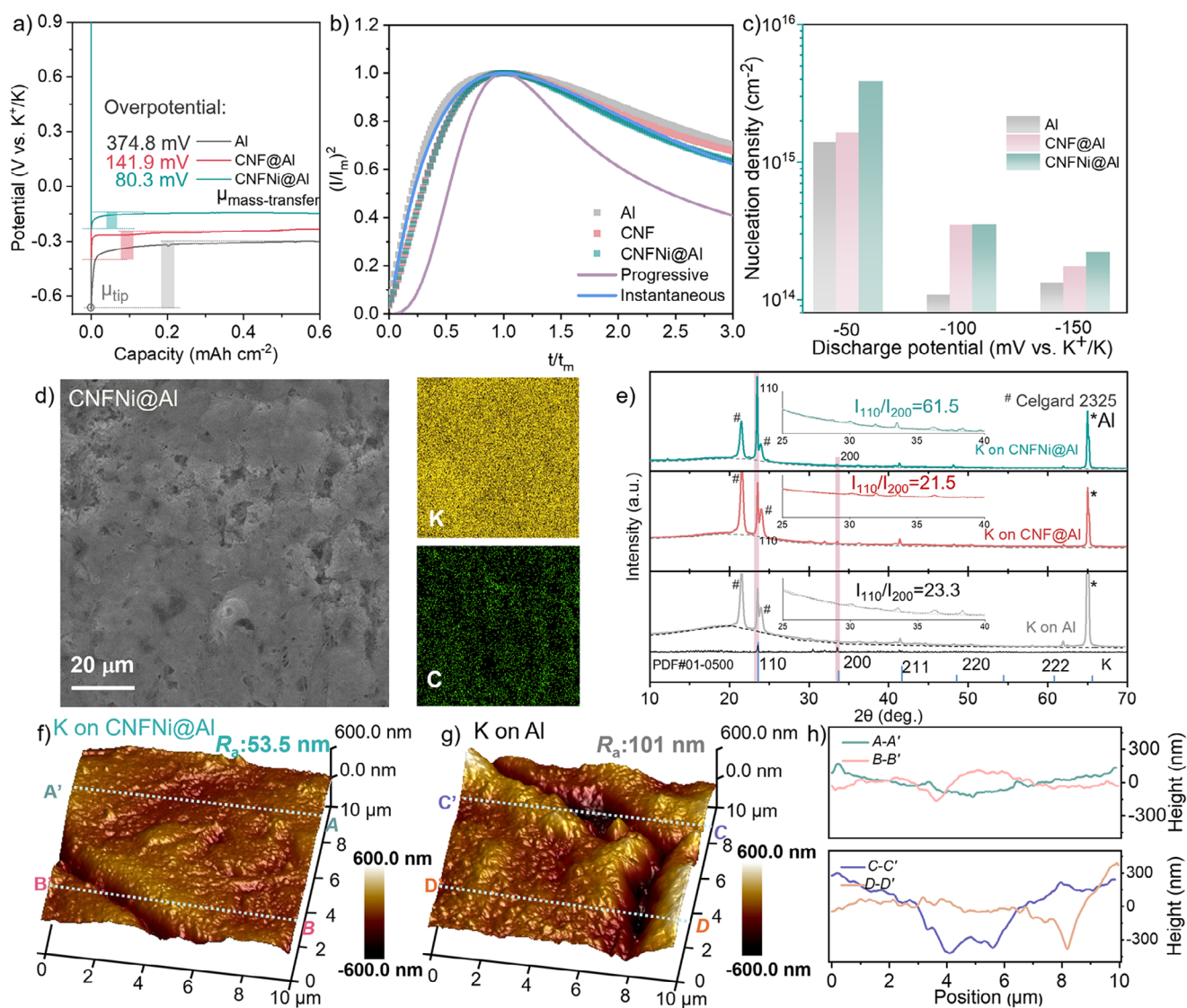


Figure 2. Nucleation behavior and plating morphology of K. a) The potential-capacity plots of K||current collector cells. b) $(I/I_m)^2 - (t/t_m)$ profiles of different asymmetric cells with different current collectors at the overpotential of -100 mV. c) Calculated nucleation density values. d) SEM images with EDS mappings of 10th-plated K on CNFNI@Al. e) XRD patterns and f, g) three-dimensional AFM topography of plated K on different substrates. h) Height variation curves on marked lines in (f, g).

in the O content of decorated Al samples further confirms the less solvent decomposition.

There are also distinct differences in organic and inorganic species of SEIs, as indicated in N1s, S 2p, and F1s spectra (Figure S9). N_xO_y and $ROSO_2^-$ from organic species account for 76% of N1s and 64% of S 2p for bare Al, which are higher than 70% and 61% for CNF@Al. These values further drastically decrease to 47% and 31% for CNFNI@Al, corresponding to an inorganic-rich SEI on CNF@Al and CNFNI@Al. Additionally, CNFNI@Al induces a greater content of K-F, K-N,^[38] KNO_3 , KNO_2 ,^[39] and K_2SO_4 in SEI as a result of $[K^+ - anion]$ reduction. Among these inorganics, the KF is typically considered to exhibit a high electron tunneling barrier, similar to the role of LiF ,^[40] which prevents continuous electrolyte consumption.

Potassium Nucleation Behaviors

We then explored the K nucleation dynamics on different current collectors (CC) in two-electrode K||CC cells. As shown in Figure 2a, the nucleation potential of Al, CNF@Al, and CNFNI@Al is 374.8, 141.9, and 80.3 mV respectively. It means a smooth K embryo generation process with a lower formation barrier for decorated Al. Moreover, the smallest mass-transfer potential of K on CNFNI@Al (Figure S10) indicates a relatively facile growth to achieve an intact planar metallic layer as well.^[41] The reason lies in the fast charge transfer in the CNFNI@Al-based cell. It exhibits the highest current exchange density of $3.82 \times 10^{-2} \text{ mA cm}^{-2}$, as determined by Tafel curves (Figure S11). To further probe the nucleation mechanism, the I-t measurements at

different overpotentials (Figure S12) were carried out. We compared the shape of normalized $(I/I_m)^2-(t/t_m)$ profiles (Figures 2b and S13–S14) with instantaneous and progressive nucleation models described by Scharifker and Hills.^[42,43] The experimental profiles for all the samples nearly coincide with the instantaneous model under different overpotentials. This suggests that the K embryo is mainly generated in the initial deposition period (Figure S15). We then calculated the nucleation density based on the following equation with the instantaneous model^[44]:

$$N = 0.065(8\pi CV_m)^{-1/2} \left(\frac{nFC}{I_m t_m} \right)^2$$

where C represents the K^+ concentration in the electrolyte; V_m is the mole volume, the mole weight divided by the density ($39.098/0.862 \text{ cm}^3 \text{ mol}^{-1}$), of deposited K; nF indicates the transferring charge ($1 \times 96\,485 \text{ C mol}^{-1}$).

It is a delight to find that the K nucleation density on CNF/Ni@Al is much greater than that of Al under different overpotentials (Figure 2c and Tables S1–S3). Abundant nuclei can provide more growth sites for the subsequent K deposition, inducing a more comprehensive and coherent K deposition layer. This aligns with the above assumption that metallic nickel and nickel-containing species decorated Al can induce a smoother nucleation process.

Scanning electron microscopy (SEM) and atomic force microscopy (AFM) were subsequently employed to detect the morphology of 10th plated K at 0.5 mA cm^{-2} for 1 mA h cm^{-2} . Upon disassembly for sample preparation, we observed numerous K dendrites penetrating the Celgard separator and trapped on the separator in the K||Al cell and several K tiny particles left in the K||CNF@Al one (Figure S16). In stark contrast, almost no K signals were discernible in the separator of CNF/Ni@Al-based cell. Additionally, CNF/Ni@Al induces a relatively compact and uniform K deposition layer with a homogenous SEI component (C atom as the presentative) over a large area (Figure 2d), while there are numerous irregular protrusions on the deposited K in the bare Al case (Figure S17). The captured pores should be related to the K dendrites left on the separator, resulting in broken SEI with limited detective C signal. Such flat deposition of K can be further explained by the extremely high intensity of K {110} plane on the CNF/Ni@Al sample (Figure 2e) compared to the bare Al and CNF@Al ones, which is likely derived from more negative adsorption energy of Ni to K, as the similar case in lithium metal batteries.^[45] In situ optical microscopy was deployed to visualize the real K plating morphology evolution. As shown in Figure S18, both Al and CNF/Ni@Al possess a flat and smooth surface at the initial stage. K dendrites and bubbles emerge on the Al foil side after 20 min deposition, and the dendrite formation becomes even more fierce after 30 min. In contrast, the plated K maintains a smooth surface on CNF/Ni@Al because of homogenous deposition. We then probed the grain size and the roughness of plated K. The deposited K on bare Al behaves as randomly aggregated tiny grains with an average diameter of $2 \mu\text{m}$. In comparison, the K on CNF@Al possesses a larger grain size of around $13 \mu\text{m}$ and a relatively planar morphology. The K

grain size is as large as $19 \mu\text{m}$ on the CNF/Ni@Al collector (Figures S19 and S20). It shows a smooth morphology with the smallest height variation and roughness (R_a) of 53.5 nm (Figure 2f–h), evidencing the facilitated nucleation process. Having demonstrated the benefits of Ni incorporation in potassium nucleation, we center mainly on the CNF/Ni@Al sample in the following discussion for clarity.

Properties of SEI on Deposited K

We further examined the composition of SEI generated on plated K layers. Similar to the findings from the previous analysis of the SEI on current collectors, XPS spectra indicate a higher content of inorganic species including S^{2-} and KNO_3 for the CNF/Ni@Al sample (Figure 3a and Figures S21–S25). Besides the species difference, a downshift is found in K 2p of the CNF/Ni@Al sample after etching (Figure S21). It comes from the appearance of strong metallic K^0 peaks, suggesting a small thickness of SEI from alleviated electrolyte decomposition. This should be attributed to the higher K plating potential (μ_{plating}) of -0.105 V for CNF/Ni@Al compared to -0.152 V for Al (Figure 1a). In addition, it is noticed that the C–O peak displays a greater proportion than C=O in the CNF/Ni@Al sample compared to that for bare Al (Figure S22).

To further identify the specific species and their distribution along with depth, time-of-flight secondary ion mass spectrometry (TOF-SIMS) measurement was employed. The organic $CH_3OSO_2^-$ signal is faint in the CNF/Ni@Al sample, but shows a noticeable intensity in the bare Al sample (The upper part of Figure 3b). Similar to XPS results, the KS and KNO_3 , resulting from anion decomposition, account for a relatively high content in the CNF/Ni@Al sample compared to those of the bare Al. More inorganic components with high ionic conductivity for SEI on deposited K would facilitate the K^+ diffusion.^[46] As a result, the impedance in SEI (R_{SEI}) of the CNF/Ni@Al-based cell is 27.1 Ohm , half of its Al-based counterpart (Figure S26). The charge transfer resistance is dramatically decreased from 2634.0 Ohm for the CNF/Ni@Al cell to 454.5 Ohm for the bare Al cell. This is further validated by the calculation results from Nyquist plots at various temperatures (Figure S27 and Table S4). The K||CNF/Ni@Al cell exhibits a lower activation energy for charge transfer, at $40.65 \text{ kJ mol}^{-1}$, half of that in the K||Al cell.

As for the K- species distribution, the density of K ions increases with sputtering but it is more uniform for the CNF/Ni@Al profile (the bottom parts in Figure 3b). The intensity of K ions reaches the maximum after sputtering 270 s for CNF/Ni@Al, compared to 640 s for Al (Figure S28), indicating a thinner SEI. It is consistent with the previous XPS result and the smaller thickness (t) obtained from AFM-based nanoindentation curves for the CNF/Ni@Al sample (Figure S29). Furthermore, for the Al sample, HCO_2K displays as a dominant component within almost depth, while C–O–K accounts for a small proportion (Figures 3b and S28). In contrast, HCO_2K and C–O–K only appear at the upper region of the modified sample, with a relatively high content of C–O–K, consistent with the aforementioned stronger C–O peak in

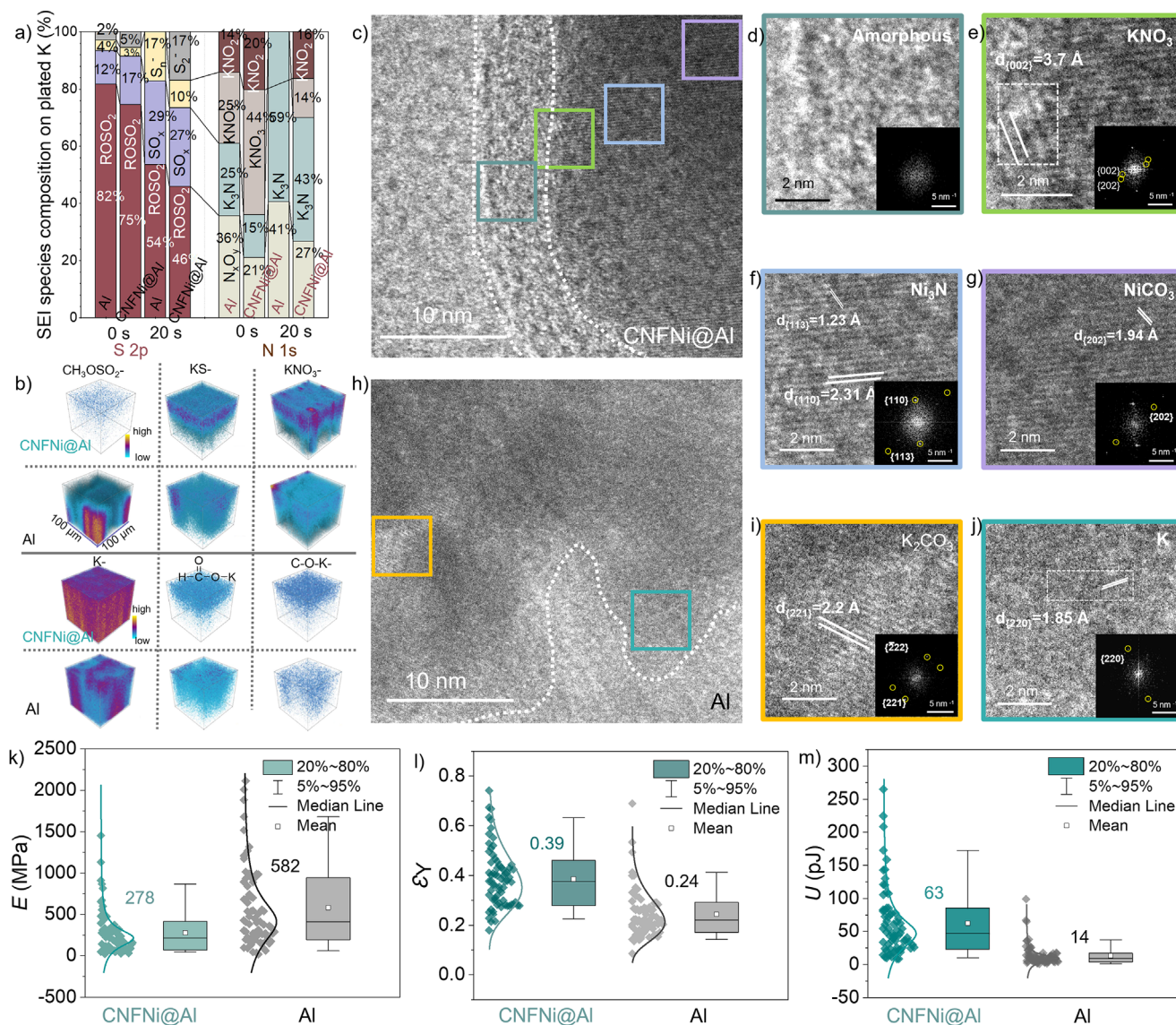


Figure 3. SEI components and mechanical properties of plated K. a) Species percentages in S 2p and N 1s spectra. b) TOF-SIMS 3D rendering images of $\text{CH}_3\text{OSO}_2^-$, KS^- , KNO_3^- , K^- , HCO_2K^- , and C-O-K^- signals. HRTEM images of SEI formed on c–g) CNFNI@Al and h–j) Al. Distribution curves of testing values of k) Young's modulus E , l) elastic strain limit ϵ_γ , and m) U values of elastic deformation of SEI on different substrates based on AFM nanoindentation measurements. The sample size is 74 and 73 for CNFNI@Al and Al, respectively.

the O 1 s spectra. It can be attributed to a more severe and deeper decomposition of DEE solvent on Al, with a lower content of elastic oligomer $[\text{CH}_2\text{OCH}_2]_n$ but a higher content of HCO_2K [47,48] as illustrated in the proposed decomposition of DEE (Figure S30).

We collect the high-resolution transmission electron microscopy (HRTEM) images of SEIs to further explore their morphology and composition. As shown in Figure 3c–e and Figure S31a–c, an almost amorphous layer with a uniform thickness of about 5 nm was generated on cycled CNFNI@Al, with a few low-crystalline inorganic species of KNO_3 . It implies that most generated inorganic species in SEI over CNFNI@Al exist in the noncrystalline state. The KNO_3 is confirmed by the lattice fringe of 3.7 Å for {002} plane and the corresponding FFT pattern of {002} and {202} planes in

Figure 3e. Apart from the lattice of KNO_3 , the most obvious fringes and FFT patterns are indexed to Ni_3N by {110} and {113} planes (Figure 3f), the bulk species of CNFNI. We speculate that the generation of low-crystalline KNO_3 was partly catalyzed by Ni_3N . Furthermore, in the bulk region, we observed the fringes of {202} plane of NiCO_3 (Figure 3g), which is not an ingredient in the initial CNFNI and should be a possible result of the interaction between the Ni species with electrolyte.[49] In stark contrast, K_2CO_3 in a size of several nanometers has been observed on the bare Al sample (Figure 3h,i and Figure S31d–f) with the {222} and {221} planes detected. It derives from deep electrolyte decomposition (Figure S30). As shown in Figure 3j, the captured lattice of 1.85 Å is well aligned with the {220} plane of K, as a potential dendrite isolated within the SEI on the Al surface.

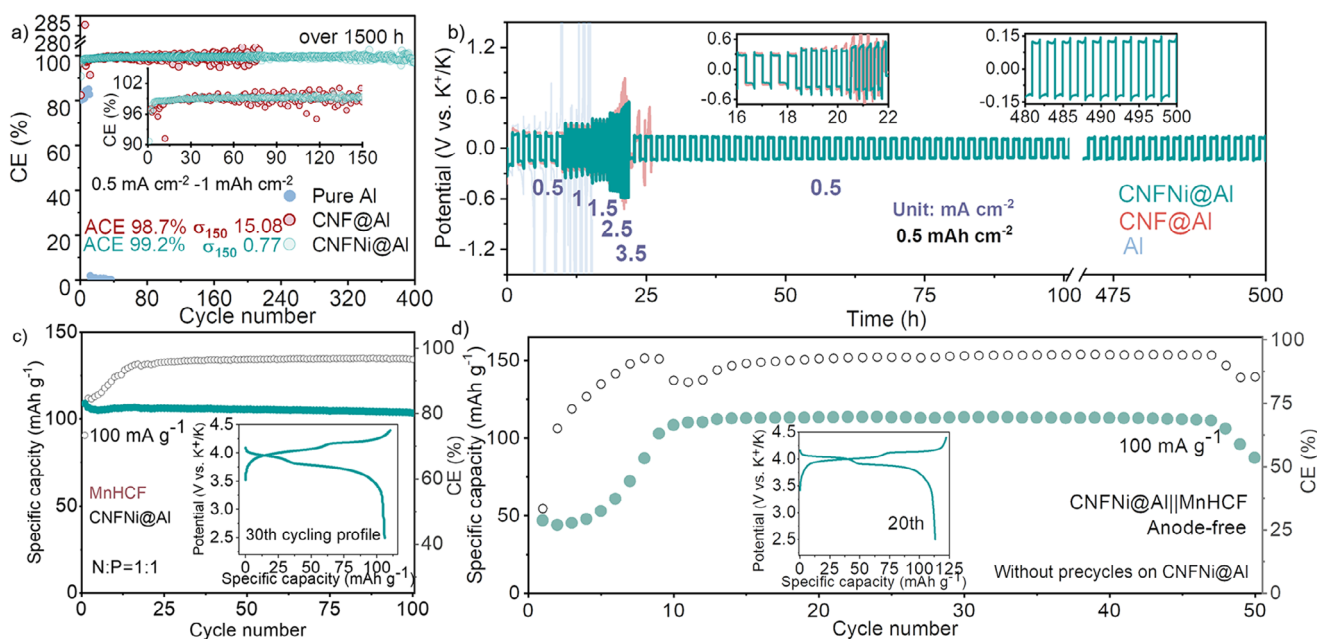


Figure 4. Reversibility in half and full cells in 1 M KFSI/DEE. a) The long-term cycling performance of asymmetric cells at 0.5 mA cm^{-2} – 1 mA h cm^{-2} . b) Rate performance of the symmetric cells. The cycling performance of MnHCF-based full cells under c) an N/P ratio of 1, and d) an N/P ratio of 0.

The SEI composition would have a great impact on the mechanical properties, which were explored through AFM-based nanoindentation tests. Three typical mechanical parameters Young's modulus E , elastic strain limit ε_Y , and the maximum energy of elastic deformation U ($U \propto E \cdot \varepsilon_Y^5$)^[30] were calculated and compared. The SEI generated on bare Al possesses a high E of 582 MPa and a low ε_Y of 0.24 (Figure 3k,l). In comparison, the CNF@Ni@Al induces an SEI with a higher ε_Y of 0.39 and a lower E of 278 MPa, implying superior elastic properties. It results from the existence of more oligomer-like species $[\text{CH}_2\text{OCH}_2]_n$ in the CNF@Ni@Al cell, which is further decomposed into HCO_2K under the continuous electron convey in bare Al counterpart,^[47,48] as indicated in XPS and TOF-SIMS results. The four times larger U value of 63 pJ for the CNF@Ni@Al sample than the Al-based one suggests increased mechanical stability in accommodating electrode swelling (Figure 3m). Therefore, this thin yet elastic SEI generated in the CNF@Ni@Al-based cell is promising to protect deposited K from parasitic reactions.

Electrochemical Performance

Benefitting from stable SEI and promoted nucleation behavior, CNF@Ni@Al induced an initial CE of 99.3%, as measured through the modified Aurbach method^[50] (Figure S32). In contrast, the bare Al and CNF@Al witness a short circuit after plating with a 2.5 mA h cm^{-2} capacity of K. The CE over 100% can be attributed to the soft-short-circuit period for CNF@Al. In terms of the long-term operation (Figure 4a), CNF@Ni@Al also endows K with an ultra-stable plating-stripping behavior of over 1500 h with an ACE over 99.2% at 0.5 mA cm^{-2} – 1 mA h cm^{-2} , outperforming 98.7% for CNF@Al. This value

is superior to nearly all the reports relying on electrodes under normal-concentration electrolytes^[51–55] (Table S5). Apart from the ACE value, the fluctuation of CE varies in different current collector-based cells, which reflects the stability of the deposition-stripping behavior of K (Insets in Figure 4a). The average standard deviation values (denoted as σ) are introduced to quantify the fluctuation degree of CE value during different cycles (Table S6). In the initial 50 cycles, the CE in the CNF@Al-based one fluctuates severely, giving rise to a high σ of 25.97%. In comparison, σ is only 1.22% in 50 cycles and further decreases to 0.61% after 300 cycles on CNF@Ni@Al, implying the smooth plating-stripping behavior of K and stable SEI. This advantage becomes even more distinct under a larger current density of 2 mA cm^{-2} (Figure S33 and Table S7). CNF@Ni@Al endows the cell with an ACE of 98.7% and a low σ value of 0.57% within 180 cycles. In contrast, the bare Al cannot tolerate this challenging current density and fails in the initial cycle owing to the limited nucleation density and large resistance. The CNF@Al-based cell exhibits an improved performance but still fails in 90 cycles.

To evaluate the rate performance, we pre-deposited K with 2 mA h cm^{-2} capacity onto different current collectors and assembled symmetric batteries. CNF@Ni@Al enables an excellent rate performance for operating at a current density of up to 3.5 mA cm^{-2} , with a small polarization compared to the Al and CNF@Al cells (Figure 4b). After the current density returns to 0.5 mA cm^{-2} , it retains stable cycling for 500 h, while the CNF@Al-based cell undergoes a sharp short-circuit within 25 h. We also examined the cycling performance at different depths of discharge (DoD) on the current collectors. The cells using CNF@Ni@Al can stably run for 800 and 200 h under 25% and 50% DoD, respectively. In contrast, the bare Al-based cells fail fast within 20 h

(Figure S34). Such superior stability under the large DoD promises a better performance in the anode-less cells.

Lastly, we assessed the performance in full-cell PMBs by coupling with typical Prussian blue cathodes. A certain amount of K metal is deposited on different current collectors to control the negative/positive capacity (N/P) ratio. We initially couple the K metal anode with a Fe-based Prussian blue (FeHCF) cathode that possesses an average discharge voltage of 3.3 V. Compared to the Al and CNF@Al-based cells with fluctuated CE and short lifetime, the CNF@Al-K||FeHCF cell (Figure S35) delivers a superior cycling performance with an ACE of 99.2% and capacity retention of 91.9% after 350 cycles under an N/P ratio of 5. Such superiority in the full cell can be also achieved when coupled with a perylene-3,4,9,10-tetracarboxylic dianhydride (PTCDA) cathode (Figure S36). We then examine the performance in high-voltage MnHCF, which is critical to realizing a high energy density. Under a low N/P ratio of 1, the CNF@Al allows stable cycling of the cell for more than 100 cycles (Figure 4c). Pushing to the limit, we tested the stability under the critical anode-free condition (N/P = 0). The CNF@Al||MnHCF cell can run for 50 cycles (Figure 4d). It displays a similar charge–discharge profile as the one using an excess K metal anode. The fluctuation in the initial 10 cycles is due possibly to the unstable SEI formed in the first several cycles. The breakage of SEI could lead to partial re-activation of isolated K, similar to the case reported in Li-metal batteries.^[56] Based on the mass of the MnHCF and the CNF@Al, an energy density of 381 Wh kg^{−1} is obtained. Such an outstanding performance has rarely been realized in anode-free PIBs using a normal-concentration electrolyte (Table S8). A high-concentration electrolyte has been widely adopted to tailor the SEI but with the sacrifice on the cost. Furthermore, it is worth mentioning that the CNF@Al current collector is directly used without precycles. On the one hand, Anode precycling is not preferred for real applications. On the other hand, it could introduce an extra K source on the anode as pointed out by Hatzell,^[57] resulting in an anode-less instead of an anode-free cell. Indeed, we observed a further improved performance (Figure S37) under the high-concentration electrolytes with precycling of CNF@Al (Figure S38). In contrast, high voltage anode-free PMBs without anode-precycling, which favors real application, have never been reported before to the best of our knowledge. Furthermore, the universality of CNF@Al is demonstrated by extending to a sodium-based system, which guarantees a high ACE of 99.91% in half cell and a superb stability of anode-free full cell (Figure S39).

Conclusion

We finely tune the surface chemistry to modify the Fermi level of the Al-based current collector. Ni-decorated CNFs are coated on the Al through a facile spray painting method, which elevates the work function of the current collector. This helps suppress the excessive electrolyte decomposition, particularly the solvent, resulting in an inorganic-rich SEI. Furthermore, potassiphilic nickel species promote nucleation behavior by increasing the densities of K embryos at

initial deposition, giving rise to much-reduced surface roughness. As a result, the K anodes based on CNF@Al realize a high CE of 99.2% with a lifetime of over 1500 h. A 4.4 V anode-free CNF@Al||MnHCF cell can be realized with 89% capacity sustained after 50 cycles at 100 mA g^{−1} without precycling the current collector and resorting to a high-concentration electrolyte. This work offers a current collector-based approach, in addition to electrolyte engineering, to tailor the SEIs for realizing stable K metal anodes.

Supporting Information

The authors have cited additional references within the Supporting Information.^[18,58–62]

Acknowledgements

The work described in this paper was substantially supported by a grant from the NSFC/RGC Joint Research Scheme sponsored by the Research Grants Council of Hong Kong and the National Natural Science Foundation of China (Project No. N_PolyU584/23 (RGC), 52361165621 (NSFC)). The authors would like to express their sincere thanks for the financial support from the Research Institute for Advanced Manufacturing (RIAM) (project code: 1-CDJU), RCNN (Project No. 1-CE0H) of The Hong Kong Polytechnic University.

Conflict of Interests

The authors declare no conflict of interest.

Data Availability Statement

The data that support the findings of this study are available from the corresponding author upon reasonable request.

Keywords: Current collector • Fermi level • Nucleation density • Potassium metal batteries • Solid electrolyte interphase

- [1] T. Hosaka, K. Kubota, A. S. Hameed, S. Komaba, *Chem. Rev.* **2020**, *120*, 6358–6466.
- [2] Y. Hu, L. Fan, A. M. Rao, W. Yu, C. Zhuoma, Y. Feng, Z. Qin, J. Zhou, B. Lu, *Natl. Sci. Rev.* **2022**, *9*, nwac134.
- [3] P. Hundekar, S. Basu, X. Fan, L. Li, A. Yoshimura, T. Gupta, V. Sarbada, A. Lakhnot, R. Jain, S. Narayanan, Y. Shi, C. Wang, N. Koratkar, *Proc. Natl. Acad. Sci. USA* **2020**, *117*, 5588–5594.
- [4] S. Li, H. Zhu, C. Gu, F. Ma, W. Zhong, M. Liu, H. Zhang, Z. Zeng, S. Cheng, J. Xie, *ACS Energy Lett.* **2023**, *8*, 3467–3475.
- [5] Z. Yu, K. Fan, Q. Liu, D. Wang, C. Chen, Y. Zhu, H. Huang, B. Zhang, *Adv. Funct. Mater.* **2024**, *34*, 2315446.
- [6] P. Liu, H. Hao, A. Singla, B. S. Vishnugopi, J. Watt, P. P. Mukherjee, D. Mitlin, *Angew. Chem. Int. Ed.* **2024**, *63*, e202402214.

- [7] H. Yang, F. He, M. Li, F. Huang, Z. Chen, P. Shi, F. Liu, Y. Jiang, L. He, M. Gu, Y. Yu, *Adv. Mater.* **2021**, 33, 2106353.
- [8] L. Fan, H. Xie, Y. Hu, Z. Caixiang, A. M. Rao, J. Zhou, B. Lu, *Energy Environ. Sci.* **2023**, 16, 305–315.
- [9] Z. Zhang, X. Wang, J. Zhu, N. Li, L. Wang, Y. Yang, Y. Chen, L. Tan, X. Niu, X. Wang, X. Ji, Y. Zhu, *Angew. Chem. Int. Ed.* **2025**, 64, e202415491.
- [10] Q. Li, G. Liu, P. Kumar, F. Zhao, Y. Wang, T. Cai, Y. Chen, H. Xie, W. Wahyudi, Z. Ma, J. Ming, *Adv. Funct. Mater.* **2025**, 35, 2416714.
- [11] P. Verma, P. Maire, P. Novák, *Electrochim. Acta* **2010**, 55, 6332–6341.
- [12] Q. T. Campbell, *J. Phys. Chem. C* **2024**, 128, 10259–10269.
- [13] L. R. F. Allen, J. Bard, *Electrochemical Methods Fundamentals and Applications*, Second ed. John Wiley & Sons, Inc., 605 Third Avenue, New York **2001**.
- [14] S. Trasatti, *Pure Appl. Chem.* **1986**, 58, 955–966.
- [15] J. Jung, J. Y. Kim, I. J. Kim, H. Kwon, G. Kim, G. Doo, W. Jo, H.-T. Jung, H.-T. Kim, *J. Mater. Chem. A* **2022**, 10, 20984–20992.
- [16] X. Lian, Z. Ju, L. Li, Y. Yi, J. Zhou, Z. Chen, Y. Zhao, Z. Tian, Y. Su, Z. Xue, X. Chen, Y. Ding, X. Tao, J. Sun, *Adv. Mater.* **2024**, 36, 2306992.
- [17] H. Huang, Y. Wang, M. Li, H. Yang, Z. Chen, Y. Jiang, S. Ye, Y. Yang, S. He, H. Pan, X. Wu, Y. Yao, M. Gu, Y. Yu, *Adv. Mater.* **2023**, 35, 2210826.
- [18] X.-L. Zhang, L. Ma, Y.-P. Cai, J. Franssaer, Q. Zheng, *Matter* **2024**, 7, 583–602.
- [19] Y. Lei, M. Chen, Y. Li, W. Zhang, D. Zhao, Q. Zhu, *Mater. Today Phys.* **2023**, 35, 101141.
- [20] S. Wang, Y. Yan, D. Xiong, G. Li, Y. Wang, F. Chen, S. Chen, B. Tian, Y. Shi, *Angew. Chem. Int. Ed.* **2021**, 60, 25122–25127.
- [21] Z. Chen, L. Wang, J. Zheng, Y. Huang, H. Huang, C. Li, Y. Shao, X. Wu, X. Rui, X. Tao, H. Yang, Y. Yu, *ACS Nano* **2024**, 18, 8496–8510.
- [22] Y. Feng, A. M. Rao, J. Zhou, B. Lu, *Adv. Mater.* **2023**, 35, 2300886.
- [23] Z. Hou, Y. Gao, R. Zhou, B. Zhang, *Adv. Funct. Mater.* **2022**, 32, 2107584.
- [24] S. Li, H. Zhu, Y. Liu, Z. Han, L. Peng, S. Li, C. Yu, S. Cheng, J. Xie, *Nat. Commun.* **2022**, 13, 4911.
- [25] R. Zhou, H. Tan, Y. Gao, Z. Hou, X. Du, B. Zhang, *Carbon* **2022**, 186, 141–149.
- [26] Y. Zhong, S. Zhou, Q. He, A. Pan, *Energy Storage Mater.* **2022**, 45, 48–73.
- [27] Y. Li, L. Zhang, S. Liu, X. Wang, D. Xie, X. Xia, C. Gu, J. Tu, *Nano Energy* **2019**, 62, 367–375.
- [28] L. Zhang, C. Liu, R. Song, Q. Wang, Y. Chen, P. Huang, *J. Porous Mater.* **2024**, 31, 1087–1099.
- [29] R. Tran, Z. Xu, B. Radhakrishnan, D. Winston, W. Sun, K. A. Persson, S. P. Ong, *Scientific Data* **2016**, 3, 160080.
- [30] Y. Gao, X. Du, Z. Hou, X. Shen, Y.-W. Mai, J.-M. Tarascon, B. Zhang, *Joule* **2021**, 5, 1860–1872.
- [31] P. Liu, Y. Wang, H. Hao, S. Basu, X. Feng, Y. Xu, J. A. Boscoboinik, J. Nanda, J. Watt, D. Mitlin, *Adv. Mater.* **2020**, 32, 2002908.
- [32] Y.-X. Lin, Z. Liu, K. Leung, L.-Q. Chen, P. Lu, Y. Qi, *J. Power Sources* **2016**, 309, 221–230.
- [33] R. Ramprasad, P. V. Allmen, L. R. C. Fonseca, *Phys. Rev. B* **1999**, 60, 6023–6027.
- [34] T. C. Leung, C. L. Kao, W. S. Su, Y. J. Feng, C. T. Chan, *Phys. Rev. B* **2003**, 68, 195408.
- [35] A. Kahn, *Mater. Horiz.* **2016**, 3, 7–10.
- [36] M. Razavy, *Quantum theory of tunneling*, World Scientific, Singapore, **2013**.
- [37] X. Ren, P. Gao, L. Zou, S. Jiao, X. Cao, X. Zhang, H. Jia, M. H. Engelhard, B. E. Matthews, H. Wu, H. Lee, C. Niu, C. Wang, B. W. Arey, J. Xiao, J. Liu, J.-G. Zhang, W. Xu, *Proc. Natl. Acad. Sci. USA* **2020**, 117, 28603–28613.
- [38] T. G. J. shama, J. D. Rimstidt, R. Staley, *Chem. Phys. Lett.* **1972**, 15, 232–235.
- [39] X. Li, Q. Li, W. Yan, B. Fan, Z. Wang, *Int. J. Hydrogen Energy* **2024**, 51, 443–451.
- [40] Q. Zhao, S. Stalin, L. A. Archer, *Joule* **2021**, 5, 1119–1142.
- [41] L. Liu, Y.-X. Yin, J.-Y. Li, S.-H. Wang, Y.-G. Guo, L.-J. Wan, *Adv. Mater.* **2018**, 30, 1706216.
- [42] B. Scharifker, G. Hills, *Electrochim. Acta* **1983**, 28, 879–889.
- [43] B. Thirumalraj, T. T. Hagos, C.-J. Huang, M. A. Teshager, J.-H. Cheng, W.-N. Su, B.-J. Hwang, *J. Am. Chem. Soc.* **2019**, 141, 18612–18623.
- [44] D. Grujicic, B. Pesic, *Electrochim. Acta* **2002**, 47, 2901–2912.
- [45] V. Pande, V. Viswanathan, *ACS Energy Lett.* **2019**, 4, 2952–2959.
- [46] R. K. Hona, A. D. Azure, M. Guinn, U. S. Phuyal, K. Stroth, A. K. Thapa, *Int. J. Mol. Sci.* **2023**, 24, 16855.
- [47] D. Aurbach, E. Pollak, R. Elazari, G. Salitra, C. S. Kelley, J. Affinito, *J. Electrochem. Soc.* **2009**, 156, A694.
- [48] Y. Yang, D. M. Davies, Y. Yin, O. Borodin, J. Z. Lee, C. Fang, M. Olguin, Y. Zhang, E. S. Sablina, X. Wang, C. S. Rustonji, Y. S. Meng, *Joule* **2019**, 3, 1986–2000.
- [49] Z. Li, L. Huai, S. Li, M. Ma, K. Luo, Y. Zhao, D. Wang, X. Sun, Z. Peng, *Energy Storage Mater.* **2021**, 37, 491–500.
- [50] B. D. Adams, J. Zheng, X. Ren, W. Xu, J.-G. Zhang, *Adv. Energy Mater.* **2018**, 8, 1702097.
- [51] P. Liu, Y. Wang, Q. Gu, J. Nanda, J. Watt, D. Mitlin, *Adv. Mater.* **2020**, 32, 1906735.
- [52] X. Tang, D. Zhou, P. Li, X. Guo, B. Sun, H. Liu, K. Yan, Y. Gogotsi, G. Wang, *Adv. Mater.* **2020**, 32, 1906739.
- [53] J. Wang, J. Yuan, C. Chen, L. Wang, Z. Zhai, Q. Fu, Y. Liu, L. Dong, W. Yan, A. Li, J. Zhang, *Nano Energy* **2020**, 75, 104914.
- [54] X. Zhao, F. Chen, J. Liu, M. Cheng, H. Su, J. Liu, Y. Xu, *J. Mater. Chem. A* **2020**, 8, 5671–5678.
- [55] M. Zhou, W. Qi, Z. Hu, M. Cheng, X. Zhao, P. Xiong, H. Su, M. Li, J. Hu, Y. Xu, *ACS Appl. Mater. Interfaces* **2021**, 13, 17629–17638.
- [56] W. Zhang, P. Sayavong, X. Xiao, S. T. Oyakhire, S. B. Shuchi, R. A. Vilá, D. T. Boyle, S. C. Kim, M. S. Kim, S. E. Holmes, Y. Ye, D. Li, S. F. Bent, Y. Cui, *Nature* **2024**, 626, 306–312.
- [57] K. B. Hatzell, *ACS Energy Lett.* **2023**, 8, 4775–4776.
- [58] J. Tafel, *Zeitschrift für Physikalische Chemie* **1905**, 50U, 641–712.
- [59] C. Zhang, Y. Xu, M. Zhou, L. Liang, H. Dong, M. Wu, Y. Yang, Y. Lei, *Adv. Funct. Mater.* **2017**, 27, 1604307.
- [60] M. Han, J. Jiang, S. Lu, Y. Jiang, W. Ma, X. Liu, B. Zhao, J. Zhang, *ACS Appl. Mater. Interfaces* **2022**, 14, 900–909.
- [61] Y. Yi, J. Li, Z. Gao, W. Liu, Y. Zhao, M. Wang, W. Zhao, Y. Han, J. Sun, J. Zhang, *Adv. Mater.* **2022**, 34, 2202685.
- [62] Y. Zhao, B. Liu, Y. Yi, X. Lian, M. Wang, S. Li, X. Yang, J. Sun, *Adv. Mater.* **2022**, 34, 2202902.

Manuscript received: January 24, 2025

Revised manuscript received: February 25, 2025

Accepted manuscript online: March 17, 2025

Version of record online: March 27, 2025